PHYSICAL REVIEW B **87**, 214418 (2013)

# Incommensurability and spin dynamics in the low-temperature phases of $Ni_3V_2O_8$

G. Ehlers, A. A. Podlesnyak, and S. E. Hahn
*Quantum Condensed Matter Division, Oak Ridge National Laboratory, Oak Ridge, Tennessee 37831-6475, USA*

R. S. Fishman
*Materials Science and Technology Division, Oak Ridge National Laboratory, Oak Ridge, Tennessee 37831-6114, USA*

O. Zaharko, M. Frontzek, and M. Kenzelmann
*Laboratory for Neutron Scattering, Paul Scherrer Institute, CH-5232 Villigen, Switzerland*

A. V. Pushkarev, S. V. Shiryaev, and S. Barilo
*Institute of Solid State and Semiconductor Physics, Minsk 220 072, Belarus*

(Received 26 April 2013; published 17 June 2013)

Magnetic order and low-energy spin dynamics in the zero field ground state of $Ni_3V_2O_8$ are revealed in elastic and inelastic neutron scattering experiments. Neutron diffraction shows that below $T = 2.3$ K the $Ni^{2+}$ moments (spin $S = 1$) order in a cycloid pattern with incommensurate wave vector $\boldsymbol{k}_{\rm ICM} = (0,1,\tau)$, where $\tau = 0.4030 \pm 0.0004$, which is superimposed on a commensurate antiferromagnetic spin arrangement with $\boldsymbol{k}_{\rm CM} = (0,0,0)$. Three spin wave modes are discerned below $E \sim 3$ meV in inelastic measurements and qualitatively described by a model Hamiltonian that involves near neighbor exchange, local anisotropy, and a small biquadratic coupling between the spine and cross-tie sites. Results from both elastic and inelastic scattering experiments suggest that the two sublattices on spine and cross-tie sites are largely decoupled.

DOI: 10.1103/PhysRevB.87.214418 PACS number(s): 75.10.Hk, 75.25.−j, 78.70.Nx

## I. INTRODUCTION

Many new multiferroic materials, in which both magnetic and electric order parameters coexist, have emerged during the last decade.[1–4] The study of these systems, and the new phenomena associated with the coupling between ferroelectric polarization and magnetic order, is driven by the immense technological promise that new types of multifunctional devices may be developed which are based on these materials, for example, for information storage.[5]

$Ni_3V_2O_8$ is a multiferroic system with an extremely rich phase diagram. To date, many experimental and theoretical studies of $Ni_3V_2O_8$ have been published in the literature, with techniques including neutron scattering, nonresonant x-ray magnetic scattering, specific heat, muon spin relaxation, $^{51}$V NMR, electric polarization, and magnetization.[6–18] $Ni_3V_2O_8$ undergoes a series of successive and complex phase transitions when cooled in zero field, and four different magnetically ordered phases have been identified below ∼9 K (which were termed, in order of decreasing temperature, HTI, LTI, C, C′). In the HTI and LTI phases, magnetic order is incommensurate, with an ordering wave vector parallel to the $H$ direction, and a spin reorientation occurs at the transition between the two phases.[10] The LTI phase shows spontaneous electric polarization which sparked a lot of interest in this compound. The paraelectric low-temperature C and C′ phases have been previously described as canted antiferromagnetic phases with commensurate order but the main difference between the two phases remained unclear.[8,13]

Magneto-optical investigations and band structure calculations show that $Ni_3V_2O_8$ is a local moment insulator and that each $Ni^{2+}$ ion carries spin $S = 1$ with 2 $\mu_B$ local moment as expected.[11] The Curie-Weiss temperature of $Ni_3V_2O_8$ is $\Theta_W \sim -30$ K,[6] and spontaneous magnetic order occurs at $T_N \sim 9$ K.[7] Thus, by a conventional estimate[19] the degree of geometric frustration in this material is moderate, as the ratio $|\Theta_W/T_N| \sim 3$ shows. However, the unusually large number of distinct zero-field phases can still be attributed to the interplay between the particular lattice geometry, which features two distinct Ni sites unrelated by symmetry, and the antiferromagnetic near neighbor interactions. The two sites have been commonly referred to as "spine" (Wyckoff notation 8*e*) and "cross-tie" (4*a*) respectively, their atom positions in the unit cell can be found in Table I.

In this paper the magnetic interactions in $Ni_3V_2O_8$ are being studied with elastic and inelastic neutron scattering measurements, and with supporting model calculations based on a magnetic Hamiltonian that contains exchange and anisotropy terms. Despite a large body of work, an understanding of $Ni_3V_2O_8$ at this level has been missing so far. In particular, the difference between the magnetic ordering patterns in the C and C′ phases can now be understood.

## II. EXPERIMENT

Single crystals of $Ni_3V_2O_8$ were grown from a melt of $BaO/1.17{\cdot}V_2O_5$ composition, which is between two eutectic points on the $BaO/V_2O_5$ phase diagram.[20] The starting materials $BaCO_3$, NiO, and $V_2O_5$ (all in powder form and of 99.99% purity) were mixed in molar ratio 1:1:1.5 and placed in a platinum crucible. The mixture was calcined in air at 900 °C. After homogenization of the melt at 1200 °C for 8 h, the temperature in the furnace was decreased down to approximately 900 °C. The remainder of the flux melt was removed from the crucible and grown crystals were cooled down to room temperature at the rate 50 °C/h for about 15 h. Typical crystals were of deep dark gray color and had a

 

TABLE I. Relative atomic coordinates of atoms of $Ni_s$ (spine) and $Ni_c$ (cross-tie) sites used with Table V in Ref. 10 and tables below.

| Atom | x | y | z |
|---|---|---|---|
| $Ni_{s1}$ | 0.25 | 0.13 | 0.25 |
| $Ni_{s2}$ | 0.75 | 0.37 | 0.75 |
| $Ni_{s3}$ | 0.25 | 0.37 | 0.75 |
| $Ni_{s4}$ | 0.75 | 0.13 | 0.25 |
| $Ni_{c1}$ | 0.00 | 0.00 | 0.00 |
| $Ni_{c2}$ | 0.00 | 0.50 | 0.50 |

rhombic plate habit with up to 2 $cm^2$ square surface of the main rhombic face of the {010} type and a thickness along the $b$ axis in the range 1–3 mm. For well shaped single crystals the $a$ and $c$ axes coincided well with the rhombic face diagonals. X-ray fluorescent analysis confirmed a desirable cation ratio in the grown crystals as well as absence of barium at the level of the detection limit. The orthorhombic space group *Cmca* at room temperature and lattice parameters $a = 5.931(6)$ Å, $b = 11.374(8)$ Å, $c = 8.235(5)$ Å were determined with x-ray powder diffraction of several samples prepared from crushed single crystals, and found to be in good agreement with previously published data.[10]

Neutron diffraction experiments were performed at the TRICS instrument at SINQ, Switzerland.[21] Measurements were set up at a neutron wavelength of $\lambda = 2.317$ Å in normal beam geometry (PG monochromator, PG filter), using a lifting-arm $^3$He tube detector. The crystal was mounted in an orange cryostat with base temperature of $T = 1.4$ K. In total 309 of the incommensurate (see below) reflections were measured, 229 of them being independent. For antiferromagnetic and ferromagnetic commensurate refinements 30 and 149 reflections were used, respectively.

Inelastic neutron scattering experiments were carried out at the Cold Neutron Chopper Spectrometer (CNCS) at the Spallation Neutron Source (SNS) in Oak Ridge.[22] The sample was again mounted in an orange cryostat with a base temperature of $T = 1.8$ K. Two series of scans were made, one in $(0KL)$ and the other in $(HK0)$ scattering geometry. Detector coverage out-of-plane was about $\pm 15^\circ$, so that a limited $Q$ range out-of-plane could be accessed. Two settings for the incident energy were chosen: (i) To obtain a map of the elastic scattering in a larger $Q$ range, $E_i = 12$ meV was used ($\lambda_i = 2.61$ Å) with an energy resolution at the elastic line of $\Delta\hbar\omega = 0.51$ meV full width at half maximum (FWHM), and (ii) to measure the low energy spin waves $E_i = 3.3$ meV was used ($\lambda_i = 4.98$ Å) with an energy resolution at the elastic line of $\Delta\hbar\omega = 0.067$ meV (FWHM).

## III. ELASTIC SCATTERING RESULTS

An elastic scattering map measured at CNCS at $T = 1.8$ K in the C′ phase [in the $(0KL)$ plane] is shown in Fig. 1, revealing incommensurate Bragg peaks at positions $L = \pm 0.4$ relative lattice units (r.l.u.).

After a least-squares refinement of the several hundred peak intensities measured at TRICS, which was performed with the FULLPROF suite,[23] the following model for the magnetic structure at $T = 1.8$ K emerges. There is a commensurate

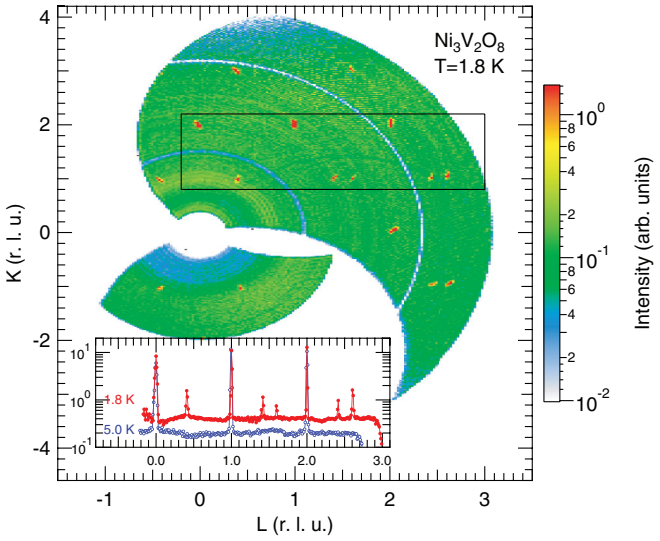


FIG. 1. (Color online) Elastic neutron scattering map obtained at CNCS in the C′ phase at $T = 1.8$ K, with the $(0KL)$ plane chosen as the scattering plane. Incommensurate peaks at $L = \pm 0.4$, where $K$ is odd, are of magnetic origin and a characteristic feature of the C′ phase (i.e., absent in higher temperature phases). Some of these new incommensurate magnetic peaks appear absent, but in fact these peaks have a very small nonzero structure factor. For example, according to the refined model, the (0,1,0.6) peak is about 12 times weaker than the the (0,1,0.4), which is consistent with the CNCS data. The inset at the bottom left of the figure shows a cut integrated in the boxed area of the plot (red filled circles). For comparison the same cut at $T = 5.0$ K is also shown (blue open circles), revealing the absence of the incommensurate peaks in a different phase at higher temperature.

part of magnetic order (CM) that persists from the C phase at higher temperature, $T \sim 4$ K, and an incommensurate part (ICM) that appears at $T = 2.3$ K and below. The CM component can be described by the wave vector $\boldsymbol{k} = (0,0,0)$ and has antiferromagnetic (AFM) as well as ferromagnetic (FM) contributions. The ICM component orders with the wave vector $\boldsymbol{k}_{\rm ICM} = (0,1,\tau)$, where $\tau = 0.4030 \pm 0.0004$, which will be discussed further below.

The AFM CM component causes new reflections $(HK0)$ to appear with integer $H, K$, where both $H$ and $K$ are odd, which break the general reflection condition (due to the $a$-glide plane) that both $H$, $K$ must be even for nuclear Bragg reflections. The FM CM component leads to increased intensities of some nuclear reflections compared to the paramagnetic phase. The CM component is the best refined within the $\Gamma_7$ irreducible representation (IRR), see Table V in Ref. 10. Magnetic moment components causing this part of the ordering are mostly on the spine Ni site (see Table I for the atomic coordinates), the values are $\mathbf{m}_s^{\rm CM} = (1.36(1),0,0.25(8))\ \mu_B$/Ni (spine site) and $\mathbf{m}_c^{\rm CM} = (0,0.07(2),-0.04(9))\ \mu_B$/Ni (cross-tie site).

The ICM component can be described with the wave vector $\boldsymbol{k}_{\rm ICM} = (0,1,\tau)$, where $\tau$ changes with temperature, see Fig. 2. Correspondingly, it leads to the appearance of Bragg peaks where $H + K$ is an odd integer, and $L = \pm 0.4$ (fractional part of $L$). In this case $\boldsymbol{k}_{\rm ICM}$ and $-\boldsymbol{k}_{\rm ICM}$ are not equivalent, and each of them generates two arms. There are four possible models of magnetic ordering based on the symmetry analysis (see Table II) and the $\Gamma_4$ IRR gives the best refinement result

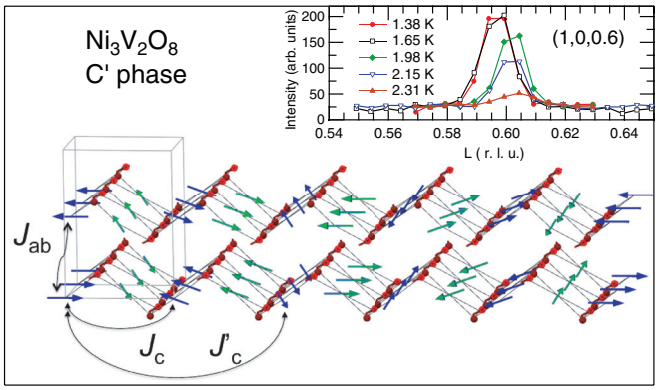


FIG. 2. (Color online) Real-space representation of the magnetic structure. The $c$ axis is horizontal and the $b$ axis is vertical. One unit cell is marked with gray lines. Cross-tie moments of the two cycloids are blue and green, spine moments are red. The three main magnetic exchange paths in the cross-tie lattice are also marked. The inset gives diffraction scans over the $(1,0,1-\tau)$ reflection which clearly show a temperature dependence and incommensurability below the phase transition into the C′ phase.

(Table III). The ICM component mainly corresponds to the cross-tie sites, the magnetic Fourier components are $\mathbf{m}_s^{\mathrm{ICM}} = (0,0.24(3)i,-0.45(4))$ $\mu_B$/Ni (spine site) and $\mathbf{m}_c^{\mathrm{ICM}} = (0,0.67(3)i,1.37(3))$ $\mu_B$/Ni (cross-tie site). Here $i$ denotes orthogonality of the $y$ and $z$ components. One notes that, according to this model, the modulation of the cross-tie magnetic moment is elliptical.

A real-space representation of the magnetic structure is given in Fig. 2. According to the analysis of the peak position, $\tau = 0.4030 \pm 0.0004$ at base temperature. This analysis involved the positions of several hundred Bragg peaks measured at TRICS, so it can be concluded with very high confidence that the ground state structure is incommensurate. Peak positions of the CNCS measurement depicted in Fig. 1 are consistent with $\tau = 0.403 \pm 0.003$.

## IV. THEORETICAL MODELING OF THE SPIN DYNAMICS

The model developed for the spin dynamics calculation makes two simplifying assumptions. First, it was assumed that magnetic order on the cross-tie site is commensurate with a fivefold increase of the unit cell length along the $c$ direction (in other words, the $c^*$ component of the magnetic wave vector $\boldsymbol{k}_{\mathrm{ICM}}$ equals 0.4 exactly). Second, moments on the spine site are antiferromagnetically aligned along the $a$ axis. The 10° tilt towards the $c$ axis obtained from the analysis of the diffraction data was neglected as was the minor incommensurate modulation of the moment direction on the spine site. Thus, in the spin dynamics calculation, the ICM/CM components will be exclusively associated with the cross-tie/spine sites, respectively.

TABLE II. Irreducible representations for the wave vector $\boldsymbol{k} = (0,1,\tau)$, phase factor $a = \exp(i\pi\tau)$.

| | | Symmetry operators | | |
|---|---|---|---|---|
| | | $2_z$ | cy | mx |
| $\Gamma_1$ | 1 | a | −a | −1 |
| $\Gamma_2$ | 1 | a | a | 1 |
| $\Gamma_3$ | 1 | −a | −a | 1 |
| $\Gamma_4$ | 1 | −a | a | −1 |

TABLE III. Relation between magnetic moment components for the $\Gamma_1$ to $\Gamma_4$ irreducible representations, space group *Cmca*, and wave vector $\boldsymbol{k} = (0,1,\tau)$. The multiplication phase factor given in Table II is omitted.

| | $\Gamma_1$ | $\Gamma_2$ | $\Gamma_3$ | $\Gamma_4$ |
|---|---|---|---|---|
| $\mathrm{Ni}_{s1}$ | $(u,v,w)$ | $(u,v,w)$ | $(u,v,w)$ | $(u,v,w)$ |
| $\mathrm{Ni}_{s2}$ | $(-u,-v,w)$ | $(-u,-v,w)$ | $(u,v,-w)$ | $(u,v,-w)$ |
| $\mathrm{Ni}_{s3}$ | $(u,-v,w)$ | $(-u,v,-w)$ | $(u,-v,w)$ | $(-u,v,-w)$ |
| $\mathrm{Ni}_{s4}$ | $(-u,v,w)$ | $(u,-v,-w)$ | $(u,-v,-w)$ | $(-u,v,w)$ |
| $\mathrm{Ni}_{c1}$ | $(0,u,v)$ | $(u,0,0)$ | $(u,0,0)$ | $(0,u,v)$ |
| $\mathrm{Ni}_{c2}$ | $(0,-u,v)$ | $(-u,0,0)$ | $(u,0,0)$ | $(0,u,-v)$ |

Ni spins ($S = 1$) on the cross-tie site order in two cycloids, each with a period of ∼5 lattice constants along the $c$ direction. One cycloid rotates clockwise within the $bc$ plane and the other rotates counterclockwise. A Dzyaloshinskii-Moriya (DM) interaction with **D** pointing along $a$ for one cycloid and along $-a$ for the other could generate this type of spin configuration. However, the DM interaction is usually very weak, an order of magnitude smaller than the exchange interactions. Therefore, the DM interaction would be expected to produce a cycloid with a very long period, much longer than the short period observed in $Ni_3V_2O_8$. On the other hand, it is noted that counter-rotating cycloids are fully consistent with the symmetry of the crystal in the presence of the observed magnetic ordering wave vector. The magnetic interactions stabilizing the magnetic structure do not require an additional symmetry breaking as is the case in the ferroelectric phase. Consequently, each cycloid was modeled by taking AFM interactions $J_c$ (between **R** and $\mathbf{R} + c\mathbf{z}$, where **R** is an atom position) and $J_c'$ (between **R** and $\mathbf{R} + 2 \cdot c\mathbf{z}$) along $z$. This results in a cycloid with wave vector $Q_z$ given by

$$\cos(Q_z c) = -\frac{J_c}{4J_c'}. \quad (1)$$

The observed wave vector $Q_z c = 0.8\pi$ is used to set $|J_c'/J_c| = 0.309$. The cross-ties are also considered to have exchange interactions $J_a$ along the $a$ axis and $J_b$ along the $b$ axis, but both turn out to be zero. Different layers separated by $b$ interact with AFM exchange $J_{ab}$ (taken between **R** and $\mathbf{R} + 1/2 \cdot a\mathbf{x} + 1/2 \cdot b\mathbf{y}$). In addition, an easy-plane anisotropy $E_a$ is included in the model to keep the cross-ties in the $bc$ plane.

Ni spins ($S = 1$) on the spine site are antiferromagnetically ordered along the $a$ axis. Because they are aligned perpendicular to the cross-ties, a biquadratic coupling $J_{bq}$ is taken between the spines and cross-ties. The spine site spins interact with AFM exchange interactions $K_a$ along the $a$ axis, $K_b$ along the $b$ axis, and $K_c$ along the $c$ axis. A $K_a'$ term for next nearest neighbors along the $a$ axis was also included, and an easy axis anisotropy $D_a$ for the spines along the $a$ axis. Thus the

Hamiltonian can be written as

$$\mathcal{H} = -\sum_{ij} J_{ij}\mathbf{S}_i \cdot \mathbf{S}_j - \sum_{ij} K_{ij}\mathbf{S}'_i \cdot \mathbf{S}'_j + J_{bq}\sum_{\langle i,j\rangle}(\mathbf{S}_i \cdot \mathbf{S}'_j)^2 + E_a \sum_i S^2_{ix} - D_a \sum_i S'^2_{ix}, \quad (2)$$

where $\mathbf{S}_i$ are the cross-ties and $\mathbf{S}'_i$ are the spines. The only interaction between the cross-ties and spines is given by the biquadratic coupling $J_{bq}$. Because $E_a$ keeps the cross-ties in the $bc$ plane, $J_{bq}$ indirectly also helps to keep the spines aligned along the $a$ axis.

To formulate the equations of motion, a unit cell with 60 sites is taken: 10 cross-ties in each of two layers, and 20 spines in each of two layers. Using a methodology outlined earlier,[24] both the mode frequencies and intensities are evaluated. The latter is essential considering that there may be as many as 120 modes per $\boldsymbol{Q}$ point. To ensure that the best fit—within the vast parameter space of the model considered here—was found, a two-step strategy was employed. Modes were first calculated at a small number of high-symmetry points in $\boldsymbol{Q}$ space and compared to the data. This allowed for fast searching through large ranges for all parameters. In a second step model parameters were then refined by analyzing cuts through the data along high symmetry directions as shown in the next section. The overall best fit to the data, discussed in the next section, is achieved for the following parameter values: $J_c = -0.20$ meV, $J'_c = -0.062$ meV, $J_{ab} = -0.02$ meV, $K_a = -1.00$ meV, $K'_a = -0.45$ meV, $K_b = -0.22$ meV, $K_c = -0.10$ meV, $J_{bq} = -0.05$ meV, $E_a = +3.00$ meV, and $D_a = +0.13$ meV.

It is noted that the calculation can be split to handle the two sites separately (cross-ties and spines) with little overall change, because the only connection between the two sites is the weak biquadratic coupling. This enabled us to identify which modes are caused by which site, an assignment which one can also make from arguments based on symmetry.

## V. INELASTIC SCATTERING RESULTS

Figure 3 shows the magnetic Bragg peak positions that were covered in the high resolution inelastic measurements at CNCS. In the $L$ direction the range $\pm 0.6$ r.l.u. was fully covered. The figure also shows how the first Brillouin zone of the magnetic lattice intercepts the plane. Cuts of the spin wave spectrum along different directions in reciprocal space are discussed below, starting with the sublattice of the cross-ties.

Figure 4 shows a cut through the inelastic spectrum $S(\boldsymbol{Q},\omega)$ along a straight line through the Γ and $S$ points, at $L = +0.4$ which is appropriate for the cross-ties. The integration depth in the perpendicular direction along $H$ was 0.1 r.l.u. The top left shows the data at base temperature, $T = 1.8$ K in the C′ phase, and the top right at $T = 3.0$ K in the C phase. While the spin wave spectra look much the same at the two temperatures, the main difference between the two phases is the absence of Bragg peaks at $L = +0.4$ in the C phase. The bottom right panel shows the computed spin wave spectrum. Since the model calculation gives the spin waves without energy or

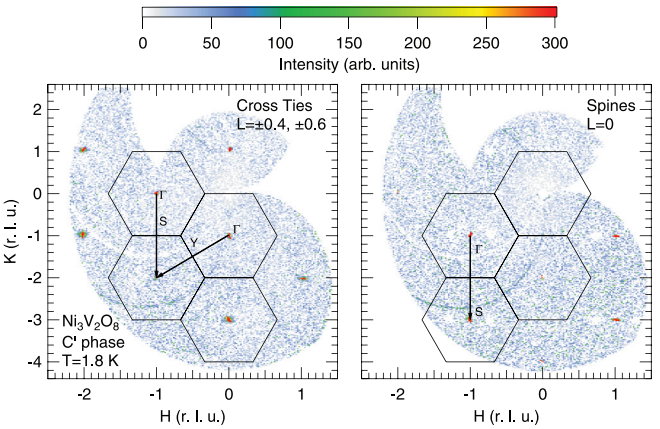


FIG. 3. (Color online) Location of magnetic Bragg peaks in the $(HK0)$ plane, at CNCS in the high resolution setting at 3.3 meV, with finite coverage in the out-of-plane direction. Peaks due to moments on the cross-tie lattice (left panel) obey $H + K =$ odd, while peaks due to moments on the spines (right panel) are at $L = 0$ and obey $H + K =$ even. Data are elastic scattering only, integrated over energy transfer $\pm 0.07$ meV. The figure also depicts the intersection of the magnetic Brillouin zone with the $L = 0$ plane and shows how cuts are taken that are discussed further below. For the two lattices the zones are shifted by 1 r.l.u. in the $K$ direction. Here Γ denotes the magnetic zone center.

$Q$ resolution, the computational results were convoluted with both energy and directional $Q$ resolution corresponding to the

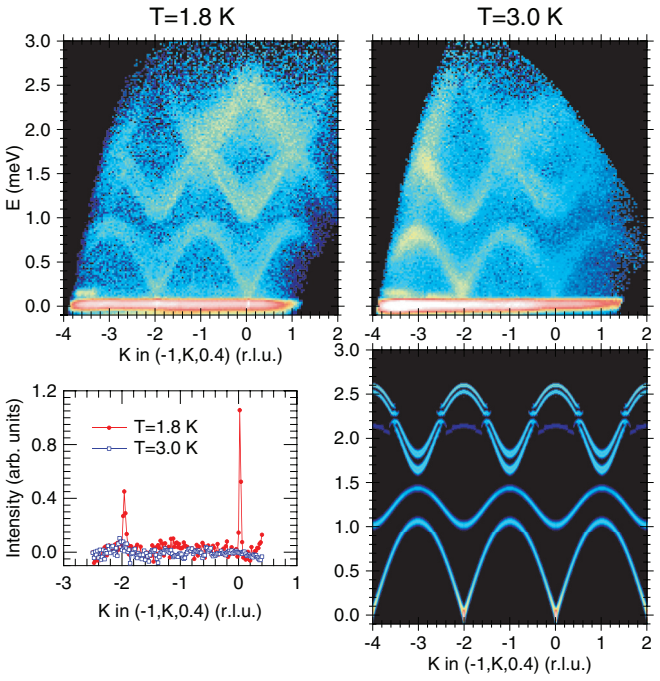


FIG. 4. (Color online) Spin waves along the $(-1, K, +0.4)$ direction through the Γ and $S$ points. Top row panels: Data in the C′ and C phases at $T = 1.8$ K and $T = 3$ K. Bottom right: Model of the spin wave spectrum. Bottom left: Cuts along $K$ at the elastic line, showing the absence of the magnetic Bragg peaks in the higher temperature phase. These cuts are background corrected with a reference measurement, so the baseline is at zero.

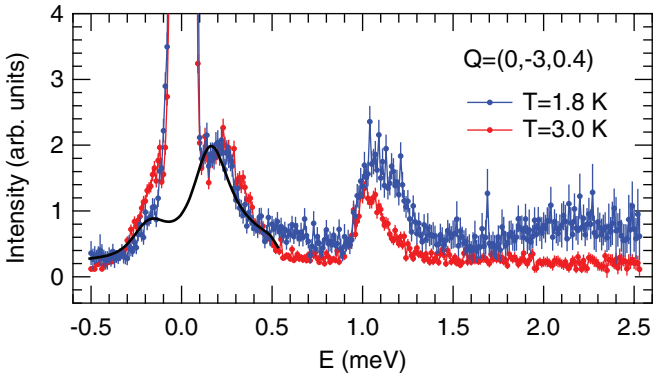


FIG. 5. (Color online) Cuts through the spin waves at a particular $\boldsymbol{Q}$ along the energy axis. The solid trace is a fit to pair of Lorentzian lines at $\pm 0.2$ meV folded with the energy resolution as measured.

experimental conditions. The resolution was computed from base principles that apply to direct geometry time-of-flight spectrometers.[22]

Comparing the data and the model calculation, several observations can be made. The lowest mode is gapped (see below) and extends up to $\sim$1.0 meV at the zone boundary (the $S$ point). A second mode is seen between $\sim$1.0 and $\sim$1.7 meV and comes out of the model calculation a little too low. A pair of modes seen between $\sim$1.8 and $\sim$2.5 meV is "out of phase" along the $K$ direction, which means that it must be associated with the spines rather than the cross-ties, because, as Fig. 3 shows, the magnetic Brillouin zone for the spine lattice is shifted by 1 r.l.u. in the $K$ direction. A cut at $L = 0$ is more appropriate for spine modes and will be discussed further below. Finally, it can also be seen that the modes as measured are somewhat broader than expected. This will be discussed in Sec. VI.

Particular attention was given to the question whether or not there is a gap at the zone center in the lowest mode. Figure 5 shows a cut along the energy axis at another reciprocal lattice vector position with odd $H + K$, at $\boldsymbol{Q} = (0, -3, +0.4)$. The data are consistent with a pair of low lying modes at $E_1 \sim 0.2$ meV on both sides of the elastic line. For the fit shown in the figure, a pair of Lorentzian lines at $\pm E_1$ was convoluted with the experimental resolution, and the intensities were weighted with the thermal population (Bose) factor. In a truly incommensurate order, it is plausible to see that a small easy-plane anisotropyy for the cross-tie site in the $bc$ plane would lead to a gap in the lowest spin wave mode.

In a similar manner, cuts through a line connecting the $\Gamma$ and $Y$ points are computed, modeled and displayed in Fig. 6 for both temperatures. The two lowest modes, associated with the cross-ties, extend between $\sim$0 and $\sim$0.7 meV and between $\sim$1.0 and $\sim$1.3 meV, respectively. The lowest mode associated with the spines can be seen as well.

Figure 7 shows a cut through the inelastic spectrum $S(\boldsymbol{Q},\omega)$ along a straight line through the $\Gamma$ and $S$ points for the spine lattice, at $L = 0$. Two modes due to the spines (minima at odd $K$ for $H = -1$), seen as one in the data, extend between $\sim$1.3 and $\sim$2.0 meV, whereas the model calculation has them somewhat higher, between $\sim$1.5 and $\sim$2.6 meV. A comparison

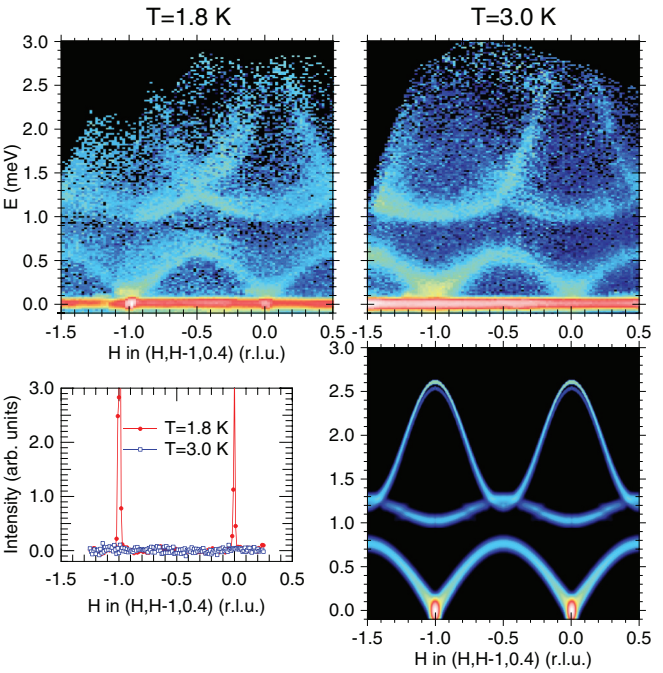


FIG. 6. (Color online) Spin waves along the $(H, H-1, +0.4)$ direction through the $\Gamma$ and $Y$ points. Top row panels: Data in the C′ and C phases at $T = 1.8$ K and $T = 3$ K. Bottom right: Model of the spin wave spectrum. Bottom left: Cuts at the elastic line, showing the absence of the magnetic Bragg peaks in the higher temperature phase. These cuts are background corrected with a control measurement, so the baseline is at zero.

with Fig. 4 suggests that these modes are not very dispersive along $L$. The lower energy cross-tie modes have moved up to around $\sim$2.0 meV. The data also show the top of one (or two) lower energy modes around $\sim$1.0 meV not reproduced in the calculation with sufficient intensity. These modes are associated with the cross-tie site, which means that the model does not reproduce their dispersion along the $L$ direction very well. This may be due to the starting assumption of commensurability along this direction.

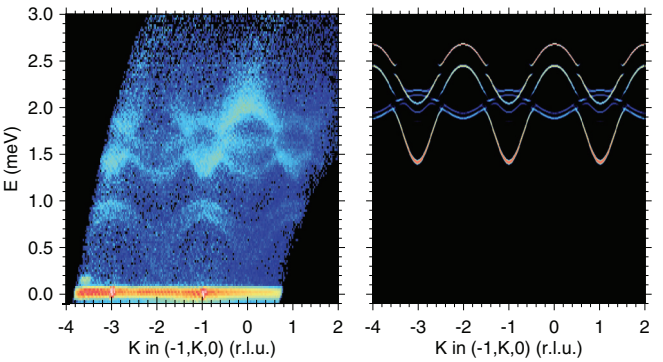


FIG. 7. (Color online) Spin waves along the $(-1, K, 0)$ direction through the $\Gamma$ and $S$ points. Left panel: Data in the C′ phase at $T = 1.8$ K. Right panel: Model of the spin wave spectrum. The lowest mode is due to the cross-ties, but the high intensity upper two modes are clearly due to the spine lattice, as their minimum is at the zone center for that lattice.

## VI. DISCUSSION

The experimental results show that a good starting point for analysis is to assume that the spines and cross-ties are independent with the exception of a weak biquadratic coupling $J_{bq}$ between them. This apparent lack of coupling between the two sites was already alluded to in Ref. 10, and is supported by our analysis of the diffraction data. The spins on the cross-tie site order in two cycloids with a period of five lattice constants along the $c$ direction, and lie in the $bc$ plane, whereas spins on the spine site are antiferromagnetically ordered along the $a$ axis. Using this model one can achieve a qualitative description of the low energy spin dynamics below $\sim$3 meV. However, the model is clearly oversimplified and the interaction between the spines and cross-ties are likely more complex.

In order to achieve a consistent modeling of the diffraction data, one must assume that cross-ties on alternate sites have cycloids with opposite helicities. Only a subset of the incommensurate Bragg peaks would be observed if the cycloids had the same helicity. Counter-rotating cycloids require that the net exchange between the two is nearly zero. In other words, cross-tie moments on the site with right-handed helicity create a near zero mean field on the neighboring cross-tie site and vice versa, by virtue of a near perfect cancellation of shorter-range exchange interactions due to the triangular arrangement of the cross-tie interactions paths. A small nonzero mean field on the cross-tie site will cause the helicities of the two cycloids to be the same, and must be overcome by a small DM interaction **D** (it must be opposite on the two cross-tie sites) in order to explain the opposite helicities. Again, the model is oversimplified in this regard, as a DM interaction has not been included.

A comparison with the experimental $Q$ and energy resolutions shows that all observed spin wave modes are significantly broadened. The finite integration range of the data in reciprocal space adds to the width as the modes are dispersive, but this cannot fully explain the observed widths. It may be concluded that in both the C and C′ phases the modes have a fairly short lifetime and short correlation length in space.

It is also unexpected to see that the phase transition between the C and C′ phases only appears in the diffraction data, through the disappearance of the incommensurate Bragg peaks, but is not visible in the inelastic measurements (the spin waves are unaltered or at best change only very subtly). As the spin waves which reflect the incommensurate $\boldsymbol{k}_{\rm ICM} = (0,1,\tau)$ wave vector are preserved in the C phase, one would also expect to see evidence, at least, for short range spatial order at the same wave vector. The associated diffuse elastic scattering is perhaps just very weak.

To summarize, quantitative modeling of elastic as well as inelastic neutron scattering data taken with a single crystal specimen of $Ni_3V_2O_8$ has been achieved with satisfactory accuracy. The focus was on the two low temperature phases of the material which had not been studied in great detail up to this point. It is revealed that the magnetic order in C′ phase is incommensurate (or near commensurate) along the $L$ direction with a magnetic propagation vector $\boldsymbol{k}_{\rm ICM} = (0,1,\tau)$, where $\tau = 0.4030 \pm 0.0004$. Both the static order and the spin dynamics observed in the scattering experiments are extremely complex and complicated models with many parameters are needed to describe the measurements. The underlying lattice geometry certainly plays a role here, as the case of the analogous spin 3/2 system $Co_3V_2O_8$ shows which also features four distinct low-temperature phases in zero field.[25]

## ACKNOWLEDGMENTS

We acknowledge the technical and scientific support from the staff at the SNS and at PSI. This work was partly performed at SINQ, Paul Scherrer Institute, Villigen, Switzerland. S.E.H. acknowledges support by the Laboratory's Directors's fund, Oak Ridge National Laboratory. R.S.F. acknowledges support by the US Department of Energy, Office of Basic Energy Sciences, Materials Sciences and Engineering Division. Research at Oak Ridge National Laboratory's Spallation Neutron Source was supported by the Scientific User Facilities Division, Office of Basic Energy Sciences, US Department of Energy.

[1] N. Hill, J. Phys. Chem. B **104**, 6694 (2000).
[2] D. I. Khomskii, J. Magn. Magn. Mater. **306**, 1 (2006).
[3] W. Eerenstein, N. D. Mathur, and J. F. Scott, Nature (London) **442**, 759 (2006).
[4] S.-W. Cheong and M. Mostovoy, Nat. Mater. **6**, 13 (2007).
[5] S. Valencia, A. Crassous, L. Bocher, V. Garcia, X. Moya, R. O. Cherifi, C. Deranlot, K. Bouzehouane, S. Fusil, A. Zobelli, A. Gloter, N. D. Mathur, A. Gaupp, R. Abrudan, F. Radu, A. Barthélémy, and M. Bibes, Nat. Mater. **10**, 753 (2011).
[6] N. Rogado, G. Lawes, D. Huse, A. Ramirez, and R. Cava, Solid State Commun. **124**, 229 (2002).
[7] G. Lawes, M. Kenzelmann, N. Rogado, K. H. Kim, G. A. Jorge, R. J. Cava, A. Aharony, O. Entin-Wohlman, A. B. Harris, T. Yildirim *et al.*, Phys. Rev. Lett. **93**, 247201 (2004).
[8] G. Lawes, A. B. Harris, T. Kimura, N. Rogado, R. J. Cava, A. Aharony, O. Entin-Wohlman, T. Yildirim, M. Kenzelmann, C. Broholm *et al.*, Phys. Rev. Lett. **95**, 087205 (2005).
[9] A. B. Harris, T. Yildirim, A. Aharony, and O. Entin-Wohlman, Phys. Rev. B **73**, 184433 (2006).
[10] M. Kenzelmann, A. B. Harris, A. Aharony, O. Entin-Wohlman, T. Yildirim, Q. Huang, S. Park, G. Lawes, C. Broholm, N. Rogado *et al.*, Phys. Rev. B **74**, 014429 (2006).
[11] R. C. Rai, J. Cao, S. Brown, J. L. Musfeldt, D. Kasinathan, D. J. Singh, G. Lawes, N. Rogado, R. J. Cava, and X. Wei, Phys. Rev. B **74**, 235101 (2006).
[12] R. P. Chaudhury, F. Yen, C. R. dela Cruz, B. Lorenz, Y. Q. Wang, Y. Y. Sun, and C. W. Chu, Phys. Rev. B **75**, 012407 (2007).
[13] T. Lancaster, S. J. Blundell, P. J. Baker, D. Prabhakaran, W. Hayes, and F. L. Pratt, Phys. Rev. B **75**, 064427 (2007).

[14]N. Wilson, O. Petrenko, G. Balakrishnan, P. Manuel, and B. Fåk, J. Magn. Magn. Mater. **310**, 1334 (2007).
[15]I. Cabrera, M. Kenzelmann, G. Lawes, Y. Chen, W. C. Chen, R. Erwin, T. R. Gentile, J. B. Leão, J. W. Lynn, N. Rogado *et al.*, Phys. Rev. Lett. **103**, 087201 (2009).
[16]F. Fabrizi, H. C. Walker, L. Paolasini, F. de Bergevin, T. Fennell, N. Rogado, R. J. Cava, T. Wolf, M. Kenzelmann, and D. F. McMorrow, Phys. Rev. B **82**, 024434 (2010).
[17]V. Ogloblichev, K. Kumagai, S. Verkhovskii, A. Yakubovsky, K. Mikhalev, Y. Furukawa, A. Gerashenko, A. Smolnikov, S. Barilo, G. Bychkov *et al.*, Phys. Rev. B **81**, 144404 (2010).
[18]J. Wang, M. Tokunaga, Z. Z. He, J. I. Yamaura, A. Matsuo, and K. Kindo, Phys. Rev. B **84**, 220407 (2011).
[19]A. P. Ramirez, Annu. Rev. Mater. Sci. **24**, 453 (1994).
[20]R. Kohlmuller and J. Perraud, Bull. Soc. Chim. Fr. **3**, 642 (1964).
[21]J. Schefer, M. Könnecke, A. Murasik, A. Czopnik, T. Strässle, P. Keller, and N. Schlumpf, Physica B: Condensed Matter **276–278**, 168 (2000).
[22]G. Ehlers, A. A. Podlesnyak, J. L. Niedziela, E. B. Iverson, and P. E. Sokol, Rev. Sci. Instrum. **82**, 085108 (2011).
[23]J. Rodríguez-Carvajal, Physica B: Condensed Matter **192**, 55 (1993).
[24]J. T. Haraldsen and R. S. Fishman, J. Phys.: Condens. Matter **21**, 216001 (2009).
[25]Y. Chen, J. W. Lynn, Q. Huang, F. M. Woodward, T. Yildirim, G. Lawes, A. P. Ramirez, N. Rogado, R. J. Cava, A. Aharony *et al.*, Phys. Rev. B **74**, 014430 (2006).